RSC Advances

PAPER

View Article Online
View Journal | View Issue

Cite this: *RSC Adv.*, 2017, **7**, 30699

In situ formation of ultrafine CoS_2 nanoparticles uniformly encapsulated in N/S-doped carbon polyhedron for advanced sodium-ion batteries†

Fei Han, *[a] Tiezheng Lv,[a] Bing Sun,[b] Wen Tang,[b] Chengzhi Zhang[a] and Xuanke Li*[ab]

A dragon fruit-like nanostructure consisting of CoS_2 nanoparticles and co-doped carbon polyhedron is effectively prepared through adjusting the pyrolysis processes of a Co-based zeolitic imidazolate framework (ZIF-67) precursor and subsequent heating sulfidation treatment. It was revealed that ultrafine CoS_2 nanoparticles with an average particle size of 8 nm are uniformly dispersed and completely encapsulated in the N/S-doped carbon matrix. Such a multifunctional architecture achieves the integration of the favorite traits of ultrafine active nanoparticles and heteroatom-doped carbon matrix, thus giving rise to much improved electron transfer and ion transport, and upholding the structural integrity of the electrode and electrode/electrolyte interface. As an anode for sodium-ion batteries (SIBs), the as-prepared CoS_2/C polyhedron electrodes exhibit high reversible capacity and good cycling stability. For example, a reversible specific capacity of 563 mA h g^{-1} and a capacity retention rate of 90% with a remaining capacity of 510 mA h g^{-1} are obtained after 100 cycles at 100 mA g^{-1}. In addition, a superior fast charge–discharge capability is also demonstrated with reversible specific capacities of 307 and 288 mA h g^{-1} at large current densities of 1500 and 2000 mA g^{-1}, respectively. These impressive results indicate that the ZIF-derived synthetic strategy is highly adaptable to design dragon fruit-like nanostructure consisting of metal compounds/carbon nanomaterials with potential applications in high performance electrochemical energy storage devices and other environmental technology fields.

Received 29th March 2017
Accepted 31st May 2017

DOI: 10.1039/c7ra03628k

rsc.li/rsc-advances

1. Introduction

As one of the promising substitutes for lithium-ion batteries (LIBs), sodium-ion batteries (SIBs) have increasingly attracted increasing research interests for large-scale energy storage systems, mainly because of the abundance of sodium resource, low cost and similar chemical properties of sodium and lithium.[1–8] Due to the 39% larger ionic radius of Na ions compared with Li ions, conventional LIBs anode materials employed for SIBs suffer from severe structural collapse caused by mechanical stress from volume change and sluggish Na ion diffusivity kinetics within active materials, thereby resulting in insufficient cycle life and low available capacity.[9,10] Therefore, the main bottleneck to realize the potential of SIBs is the exploration of appropriate anode materials with superior reversible capacity and excellent cycling stability. Recently, transition metal sulfides (TMS) have been widely regarded as promising high-capacity anode materials for SIBs due to their richer redox reaction sites.[11,12] In comparison with their counterpart-metal oxides, the metal–sulfide bond has smaller bandgap energy than the metal–oxygen bond, leading to higher electrical conductivity and better electrochemical activity.[13,14] Furthermore, the discharge product Na_2S from electrochemical sulfide-based materials possesses superior ionic conductivity than the Na_2O nanodomains from oxides reacting with sodium, thus giving rise to faster Na ion diffusion velocity.[15,16]

As a typical example, cobalt sulfides (CoS_x) can deliver high theoretical capacities of more than 600 mA h g^{-1} based on reversible conversion reactions for sodium ion storage. Among these different phases of cobalt sulfide candidates, CoS_2 (existing in nature, cattierite) possesses the highest theoretical capacity on account of the maximum S ratio, but has been rarely reported as an anode for SIBs due to the difficulty in the preparation of the pure phase by traditional solid state methods.[13,17–19] Like several other sulfide-based anode materials, the cycling stability of the CoS_2 anode is still severely plagued principally because of the large volume expansion/contraction and subsequent structure damage during the charge–discharge processes.[20–24] In addition to the structure collapse of sulfide-based electrodes, another main concern is the dissolution of the sulfur component originating from soluble polysulfide intermediates formed in the Na_2S formation/decomposition processes, thereby resulting in a loss

[a]College of Materials Science and Engineering, Hunan University, Changsha 410082, China. E-mail: feihan@hnu.edu.cn; xuankeli@hnu.edu.cn
[b]The Hubei Province Key Laboratory of Coal Conversion & New Carbon Materials, Wuhan University of Science and Technology, Wuhan 430081, China

† Electronic supplementary information (ESI) available. See DOI: 10.1039/c7ra03628k

of the sulfur component and consequent declining capacity.[25–27] Generally speaking, integrating the merits of reducing particle size of sulfides at a nanoscale and confining them in a protective carbon matrix represents an effective material-engineering strategy with improved surface-to-volume ratio, shortened transport length for Na ion and reinforced confinement effect, which not only can accommodate the huge volume change and prevent the active material loss, but also reduce the internal resistance and improve diffusion kinetics. To date, different cobalt sulfide-based nanostructures and composites have been reported. However, it is still a great challenge to uniformly encapsulate nano-scaled CoS_2 in carbon matrix with favorable sodium storage properties.

Inspired by the structure of the dragon fruit, herein, we report an effective top-down route to design and prepare ultrafine CoS_2 nanoparticles uniformly encapsulated in N/S-doped carbon polyhedron through the controlled pyrolysis of a Co-based zeolitic imidazolate framework (ZIF-67) precursor and subsequent sulfidation treatment. It is worth noting that the doped nitrogen and sulfur heteroatoms in carbon matrix originate from the *in situ* carbonization of nitrogen-rich organic ligands and carbon sulfurization reaction, respectively. Benefiting from the synergistic effect of ultrafine active nanoparticles and co-doped carbon matrix, the former was expected to buffer the huge volume expansion of CoS_2 material induced by the Na^+ insertion process and shorten electronic/ionic diffusion lengths, while the latter was anticipated to enhance charge transportation velocity, maintain the structural integrity of CoS_2 nanoparticles and prevent the dissolution of polysulfides. The CoS_2/C polyhedrons were explored as an anode material for SIBs and were found to exhibit excellent electrochemical performance in terms of reversible capacity, cycling performance and rate capability, thus demonstrating a great application potential for SIBs.

2. Experimental

2.1 Materials

2.1.1 Synthesis of ZIF-67 dodecahedrons. In a typical synthesis process, two types of clear solutions were first prepared by dissolving 12 mmol of 2-methylimidazole and 3 mmol of $Co(NO_3)_2 \cdot 6H_2O$ in 75 mL of methanol, respectively. Then, the two solutions were quickly mixed together under vigorous stirring to form a purple solution. The resultant mixed solution was continuously aged at room temperature for 24 h and subsequently, the purple precipitates were collected by centrifugation. After washing with water and ethanol for 4 times, purple powders were obtained by drying at 60 °C overnight.

2.1.2 Synthesis of CoS_2 nanocrystals in carbon matrix. The obtained ZIF-67 powders were directly heated in an argon flow at 400 °C and 600 °C. The temperatures inside the tube furnace were slowly raised from room temperature to the target temperature at a heating rate of 1 °C min^{-1}, and maintained for 2 h to obtain the pyrolysis products. These products were denoted as Co/C-400 and Co/C-600, respectively. Subsequently, 40 mg of Co/C sample and 800 mg of thiourea were placed at two separate positions in a quartz boat in a static argon atmosphere. Then, they were heated at 2 °C min^{-1} to 300 °C for 3 h to obtain the CoS_2/C samples.

2.2 Material characterization

The powder X-ray diffraction (XRD) tests were conducted on a Bruker D8 venture single crystal X-ray diffractometer with a scanning step of 0.02°. SEM (scanning electron microscopy) images were performed using a JEOL JSM-6701F scanning microscope at an accelerating voltage of 5 kV. TEM (transmission electron microscopy) observation was taken by a JEOL JEM2010F TEM and FEI Tecnai F20 system with a Cs corrector, and high-resolution TEM images were observed through a Titan G2 60-300 microscope, attached with energy-dispersive X-ray (EDX) spectroscope to investigate the elemental mapping. Raman spectra were measured on a Labram-010 confocal laser microscopy Raman spectroscopy system with 514.5 nm wavelength incident laser light. Nitrogen adsorption–desorption analyses were carried out using a Micromeritics Tristar 3000 instrument at 77 K to examine the properties of the pore structure. Thermogravimetric (TG) analysis was performed on a Discovery thermogravimetric analyzer with a ramping rate of 10 °C min^{-1} under nitrogen atmosphere. X-ray photoelectron spectroscopy (XPS) was determined by an ESCALAB 250 system with a monochromatic Al Kα source. The XPS data was calibrated with regard to C_{1s} binding energy of 284.5 eV.

2.3 Electrochemical measurements

The electrodes were prepared by mixing the as-prepared electrode material, conductive carbon black and carboxymethyl cellulose binder with a weight ratio of 8 : 1 : 1 in an ethanol/water solvent. The viscous slurry was uniformly coated on a copper foil with a doctor blade and then dried at 80 °C in a vacuum oven for 12 h. A typical active mass loading on each electrode disk was 1.5 mg cm^{-2}. Metallic sodium foil was used as both the reference and counter electrodes, and a glass fiber GF/D (Whatman) filter was employed as the separator. The electrolyte consisted of a 1.0 M solution of $NaClO_4$ in ethylene carbonate (EC)/diethylene carbonate (DEC) with a volume ratio of 1 : 1. Galvanostatic charge and discharge tests at various current densities were conducted on a battery tester (Land CT2001A) in the voltage range of 0.005–3 V. Cyclic voltammetry (CV) experiments was performed on a computer-controlled CHI660D electrochemical workstation at a scan rate of 0.1 mV s^{-1}, and all electrochemical impedance studies were operated on an Autolab PGSTAT204 electrochemical workstation from 0.01 Hz to 100 kHz.

3. Results and discussion

The fabrication procedure of ultrafine CoS_2 nanocrystals encapsulated in N/S-doped carbon matrix is schematically illustrated in Fig. 1a. Well-dispersed ZIF-67 dodecahedrons were first prepared *via* a solution precipitation method by mixing the methanol solution of cobalt salt and 2-methylimidazole at room temperature. During the thermal treatment

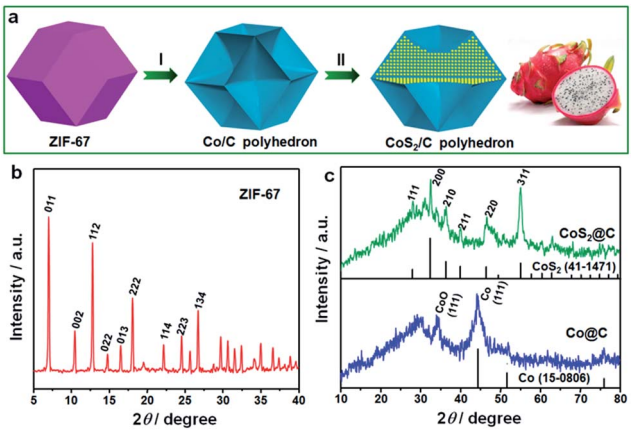

Fig. 1 (a) Schematic of the formation process of ultrafine CoS_2 nanocrystals encapsulated in doped carbon matrix. (b and c) Wide-angle XRD patterns of the (b) ZIF-67, (c) Co/C (blue) and CoS_2/C (green) polyhedrons.

process, the Co ions in ZIF-67 sample were transformed into metallic Co nanoparticles, and the organic ligands were carbonized to form carbon matrix.[28] Due to the strong confinement effect of surrounding carbon, the size of Co particles is in ultrafine nanoscale. Subsequently, the metallic Co was converted to CoS_2 nanocrystals by heating the mixture of thiourea and the abovementioned Co/C sample. Such elaborate CoS_2/C architecture is almost similar to that of a dragon fruit: ultrafine and uniformly dispersed CoS_2 nanocrystals (tiny black seeds), completely and tightly protective carbon matrix (white flesh). The dragon fruit-like architecture will play a vital role in the field of sulfide-based anode materials for SIBs.

The powder X-ray diffraction (XRD) patterns were performed to analyze the crystalline structures and the purity of the as-prepared samples. As presented in Fig. 1b, all the diffraction peaks of ZIF-67 match well with the simulated patterns reported in the previous study,[29,30] confirming the high purity and good crystallinity of ZIF-67 particles with a cubic $I\bar{4}3m$ group symmetry. In contrast to the sharp peaks of ZIF-67, the Co/C particles after pyrolysis at 400 °C exhibit less-resolved and broadened peaks. The most intense peak at 44.2° can be well attributed to the [111] lattice facets of the β-Co, associated with a standard JCPDS card no. 15-0806. On the basis of the Sherrer equation, the average particle size of Co nanocrystals was estimated to be about 4.8 nm. It is well known that Co nanoparticles, particularly ultrafine particles, are prone to be slowly oxidized in air. Thus, a weak peak of CoO at 34.1° was observed in this sample, corresponding to the [111] plane. Through the sulfidation treatment, Co particles were successfully transformed into the well-defined CoS_2 cubic phase (JCPDS: 41-1471). Six distinct diffraction peaks observed at 2θ values of 27.8, 32.3, 36.2, 39.8, 46.3 and 54.9° can be indexed to [111], [200], [210], [211], [220] and [311] crystal planes, respectively. The particle size of CoS_2 slightly increased and was calculated to be ~7.5 nm. It is worth noting that there are no evident graphite diffraction peaks, indicating the amorphous nature of carbon matrix.

The morphology and microstructure of the samples before and after pyrolysis were observed by SEM and TEM techniques. Fig. 2a and b present SEM and TEM images of the original ZIF-67 particles. The as-prepared ZIF-67 has a well-defined rhombic dodecahedral shape with smooth surface, and the particle size is uniform with an average size of about 800 nm. After subsequent pyrolysis at 400 °C, the sample well inherits the original polyhedral morphology and particle size, accompanying the invaginated particle surface (Fig. 2c and d). As shown in several TEM images, it can be seen that the Co/CoO nanoparticles were uniformly embedded and well dispersed in the carbon matrix without any severe aggregation. A high-resolution TEM image in Fig. 2f reveals the presence of ultrafine Co nanoparticles with a visible lattice fringe spacing of 0.205 nm, which is well consistent in the (111) plane of Co nanoparticles, suggesting a good agreement with the result of XRD pattern. The selected-area electron diffraction (SAED) pattern with misty rings further confirms the poor crystallinity of Co due to ultrafine nanoparticle size (Fig. 2f inset). Moreover, the pyrolysis temperature has a strong effect on the morphology of Co/C sample. While increasing the temperature to 600 °C, it was clearly observed that most Co nanoparticles broke away from the carbon matrix and sprouted out on their surface resulting in a rougher surface (Fig. S1†). The nanoparticles aggregated and grew into bigger agglomerates with serious carbon loss. This result presumably indicates that the low pyrolysis temperature of

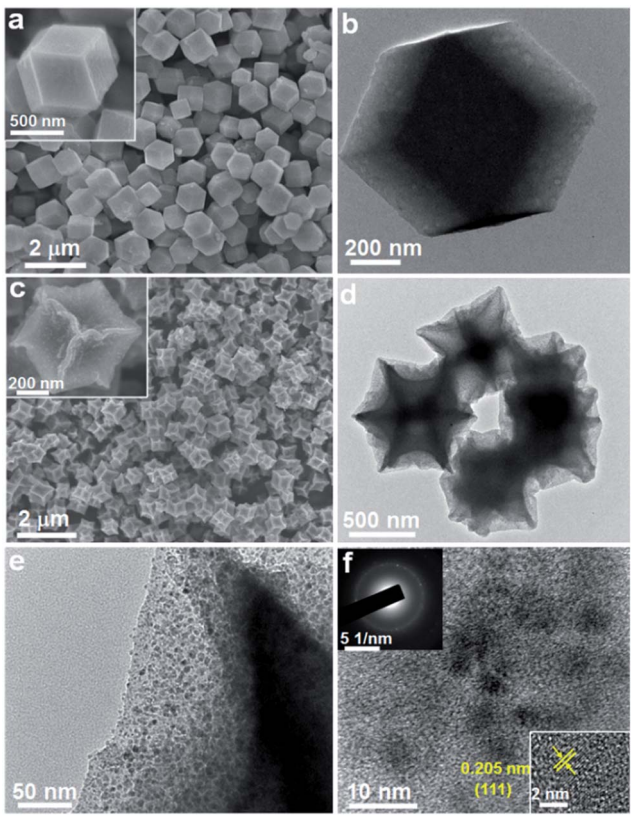

Fig. 2 SEM and TEM images of the (a and b) ZIF-67 and (c–f) Co/C sample, the inset in (f) shows the corresponding SAED pattern and magnified TEM image of Co nanoparticles.

400 °C is optimum to obtain the designed dragon fruit-like structure.

Fig. 3 presents the morphologies and elemental distribution of CoS_2/C particles. SEM and TEM images clearly reveal that the pristine morphology of Co/C is preserved perfectly without any significant changes after the sulfidation treatment. The formed CoS_2 nanoparticles are still well dispersed and encapsulated inside the carbon matrix. The CoS_2 weight in CoS_2/C polyhedrons is evaluated to be 58 wt% based on the result of the TG measurement (Fig. S2†). From a high-resolution TEM image (Fig. 3e), with closely surrounded carbon matrix, the average size of *in situ* formed CoS_2 nanocrystals is around 8 nm, which is almost close to the calculated particle size observed *via* XRD analysis. Such ultrafine nanocrystals with a uniform distribution and favorable confinement effect are extremely beneficial to increase the host ion transport velocity and release the mechanical strain by a large volume change in the anode during charge/discharge processes. A high-resolution TEM image (Fig. 3e) displays a lattice fringe with a spacing of 0.277 nm, corresponding to the [200] plane of CoS_2. The discrete and misty diffraction spots in SAED pattern further demonstrate the tiny crystal size and polycrystalline character of the CoS_2 nanoparticles (Fig. 3e, inset). The elemental mappings for CoS_2/C clearly show the co-existence and homogeneous distribution of N, Co, and S elements throughout the entire polyhedral particle based on distinguishing false color regions. It should be pointed out that the sulfur signal is derived from both the sulfur component in CoS_2 and doped sulfur atom in carbon matrix. Benefiting from the higher electronegativity, the nitrogen and sulfur heteroatoms in carbon scaffold not only immobilize CoS_2 nanoparticles to avoid aggregation, but also greatly accelerate electron transport and ion accessibility to arrive at the active sites.[31,32] On the other hand, the CoS_2/C-600 sample from Co/C-600 precursor by pyrolyzing at 600 °C exhibits irregular particle shape and serious nanoparticle aggregation, accompanied by incompletely encapsulated CoS_2 grains (Fig. S3†), indicating the significant effect of pyrolysis temperature on the morphology of the final sulfide product. To understand the effect of surface and bulk CoS_2 formation, the CoS_2/C samples were prepared through direct heating of the mixture of thiourea and ZIF-67 at 400 °C and 600 °C, respectively, and their TEM images are shown in Fig. S4.† It can be observed that their morphologies are much different from those of the samples that are subjected first to pyrolysis and then sulfidation. The polyhedron morphology cannot be well retained, and plentiful CoS_2 granules aggregate and grow outside the carbon matrix. Such a result further declares the key role of sample preparation processes in forming the final structure.

Raman spectra of Co/C and CoS_2/C polyhedrons show two dominant peaks located at 1344 and 1585 cm^{-1}, corresponding to the D and G bands of carbon matrix, respectively (Fig. 4a). The intensity ratio between D and G bands is relatively low with $I_D/I_G = 1.23$ and 1.45 for Co/C and CoS_2/C samples, respectively. With the increase of the pyrolysis temperature, the graphitization degree of carbon matrix is largely increased in Co/C-600 and CoS_2/C-600 with I_D/I_G = 0.83 and 0.94, respectively (Fig. S5a†).[33,34] It is worth noting that the values of I_D/I_G decrease slightly after a sulfidation treatment, indicating the reduced graphitization degree, further proving the successful doping of sulfur atoms in carbon backbone. The pore structures of the Co/C and CoS_2/C prepared at 400 and 600 °C were investigated by the nitrogen sorption technique, and the nitrogen sorption isotherms and pore size distribution curves are shown in Fig. 4b and S5.† The nitrogen sorption isotherm of Co/C is classified as the type IV isotherm with a typical H3 hysteresis loop, illustrating the mesoporous feature of this material.[35,36] As shown in its pore size distribution curve, it can be seen that the mesopore sizes are in two wide ranges of 2.5–18 nm and 35–70 nm (Fig. S5b†). Co/C displays an estimated BET specific surface area of 85 $m^2\ g^{-1}$ and a BJH pore volume of 0.08 $cm^3\ g^{-1}$. After

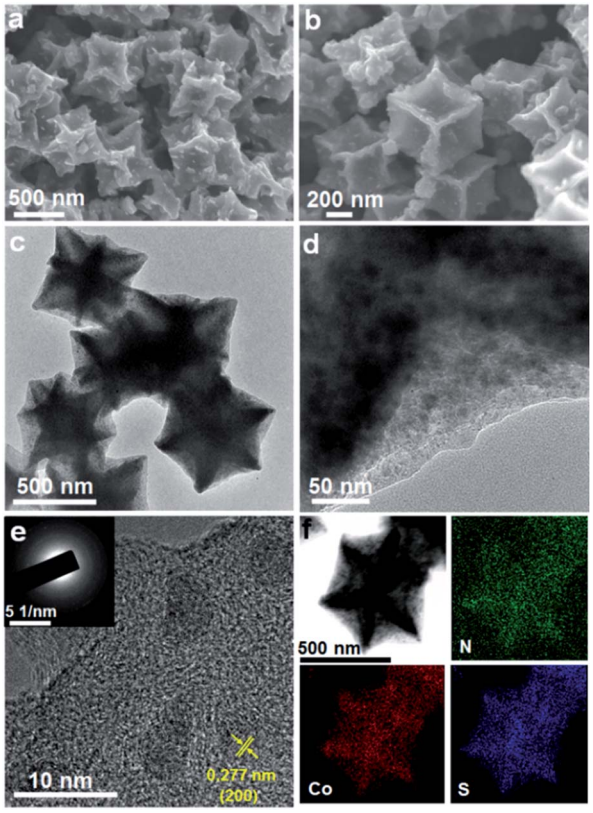

Fig. 3 The obtained product of the CoS_2/C polyhedrons: (a and b) SEM images, (c–e) TEM images (inset in (e): SAED pattern), (f) the corresponding elemental mappings.

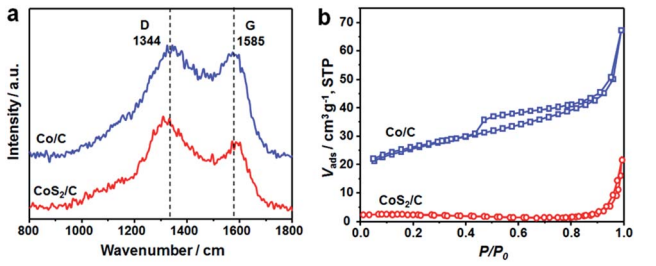

Fig. 4 (a) Raman spectra and (b) N_2 sorption isotherms of Co/C (blue) and CoS_2/C (red) polyhedrons.

sulfidation, the sample of CoS_2/C exhibits a microporous characteristic with an extremely low BET surface area of only 5.9 $m^2\ g^{-1}$. At a higher pyrolysis temperature, both the N_2 sorption isotherms of the Co/C-600 and CoS_2/C-600 are close to type-IV with a hysteresis loop. The Co/C-600 and CoS_2/C-600 show a decreased S_{BET} of 56 and 8.1 $m^2\ g^{-1}$, respectively, and their corresponding pore volumes of 0.06 and 0.04 $cm^3\ g^{-1}$.

The detailed XPS examinations were carried out to investigate the valence states of the as-fabricated CoS_2/C sample and its corresponding elements. As shown in Fig. 5a, C, O, N, S and Co elements are all observed in the survey spectrum. Compared to the characteristic peak of Co 2p, the peak of S 2p displays stronger intensity, further proving the existence of doped sulfur atom in the external carbon overlayer.[26,31] In the high-resolution Co 2p spectrum (Fig. 5b), the two main peaks centered at 781.7 and 798.9 eV correspond to spin–orbit characteristic peaks of Co $2p_{3/2}$ and Co $2p_{1/2}$ in Co–S compounds, respectively. The other peaks at 784.7 and 805.4 eV can be ascribed to the satellite peaks of Co 2p, which is an evidence for the presence of cobalt(IV).[37,38] The main S 2p peak can be divided into two characteristic peaks at 168.7 and 169.7 eV, which are possibly ascribed to C–SO_x–C groups. Another small peak located at 163.7 eV is assigned to the S $2p_{1/2}$ of S^{2-} ions matched with metal ions and the C–S_x–C (x = 1–2) functional groups, confirming the successful incorporation of the sulfur atom into the carbon framework.[31,38,39] According to the characteristic peaks of sulfur, the atomic ratio of C : doped S is calculated to be 25.2. As for N 1s core level spectrum (Fig. 5d), it can be fitted to three parts centered at 399.4, 400.6 and 401.4 eV, associating with the C–N bonds from pyridinic-N, pyrrolic-N and graphitic-N, respectively.[32,40] The pyrrolic and pyridinic N atoms can provide more active sites for charge storage and facilitate the transfer of ions in the electrode, while graphitic N atom serves as an effective electron-transfer mediator in the carbon backbone. The ratios of various N species are 30.61%, 41.73% and 27.66% for pyridinic-N, pyrrolic-N and graphitic-N, respectively, and the nitrogen content in the carbon matrix is estimated to be 12.5 atom%. Therefore, the XPS results clearly confirm the synthesis of CoS_2 in N,S-doped carbon matrix. Moreover, the EDS analysis results also show that the atomic ratios of C : N and Co : S are 7.8 and 0.6, respectively. (Fig. S6†) The nitrogen and sulfur co-doping has been demonstrated to significantly improve the electrical conductivity, thus enhancing electrochemical reaction kinetics.[41,42] Moreover, the N and S-doping can generate extrinsic topological defects in the carbon backbone and increase active sites, thus allowing higher electrochemical reaction activity.

The sodium ion storage properties of the CoS_2/C polyhedrons were assessed by various electrochemical tests in 2025-type coin cells. Fig. 6a displays its cyclic voltammograms (CVs) obtained at a scan rate of 0.1 mV s^{-1} in a potential region from 0.005 to 3 V. Two main strong peaks (1.47 and 0.52 V) are observed in the first cathodic scan. The former can be associated to the weak reduction behavior of CoS_2 with a small amount of sodium insertion following the equation $CoS_2 + xNa^+ + xe^- \rightarrow Na_xCoS_2$ (A), which usually occurs in ultrafine active nanoparticles.[31,43] The latter cathodic peak at 0.52 V is ascribed to the formation of a solid electrolyte interphase (SEI) film on the surface of an anode and the electrochemical reduction process of Na_xCoS_2 to Co nanoparticles in Na_2S matrix according to the following equation: $Na_xCoS_2 + (4-x)Na^+ + (4-x)e^- \rightarrow Co + 2Na_2S$ (B).[44] After the first scan, the two reduction peaks are shifted and divided to three current peaks at 1.47, 0.85 and 0.51 V. This behavior can be attributed to strain and structure changes from structural rearrangement and electrochemical activation in the initial sodiation process. During the anodic scan processes, several oxidation peaks in 1.75–2.06 V are related to the reverse processes of eqn (A) and (B). In contrast, the anodic current peaks and initial cathodic current peaks in the CVs of the CoS_2/C-600 sample (Fig. S7†) is much different from those of the CoS_2/C polyhedrons, which may be on account of the difference in particle size, affirming the significance of ultrafine nanoparticles in sodium storage properties. Fig. 6b depicts the representative discharge/charge voltage profiles of CoS_2/C polyhedrons for the 1st, 2nd, 10th, 30th, 50th and 100th cycles in the voltage range of 0.005–3 V. The voltage profiles agree well with the CVs in terms of voltage plateaus and their variation. The discharge and charge specific capacities in the first cycle were estimated to be 776 and 563 mA h g^{-1}, respectively, equivalent to a Coulombic efficiency of 70%. It is well known that the initial Coulombic efficiency relies heavily

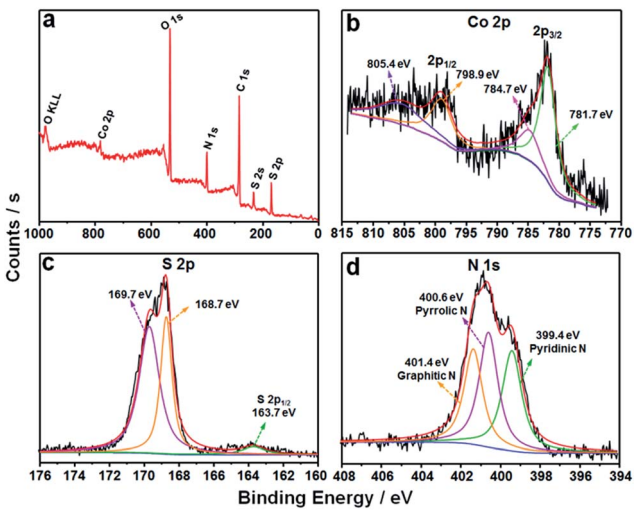

Fig. 5 (a) XPS survey spectrum of the CoS_2/C polyhedrons, and their corresponding high resolution spectra (b) Co 2p, (c) S 2p and (d) N 1s.

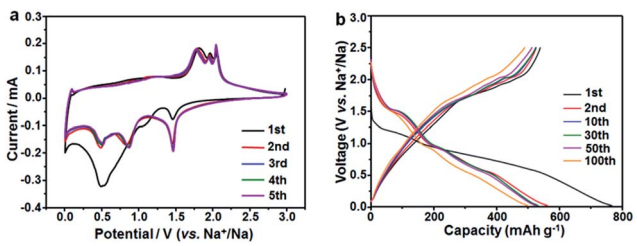

Fig. 6 Electrochemical properties of the CoS_2/C polyhedron anodes: (a) cyclic voltammograms at 0.1 mV s^{-1} and (b) galvanostatic charge/discharge profiles at 100 mA g^{-1}.

on the active particle size; smaller the size, lower the initial efficiency. The Coulombic efficiency of the CoS_2/C with only 8 nm particle size is much superior to other reported nano-scaled anode materials for SIBs.[45–47] The improved initial efficiency is mainly due to the complete encapsulation of CoS_2 nanoparticles in doped carbon matrix. Notably, the Coulombic efficiencies increased rapidly and stayed above 98% throughout the remaining cycles. From the second cycle onwards, the discharge and charge voltage profiles almost overlapped with each other, thus suggesting the excellent electrochemical reversibility of the CoS_2/C polyhedrons.

To illustrate the structural superiority of the ultrafine active nanoparticles with uniform dispersion and N/S co-doped carbon matrix of the CoS_2/C polyhedrons as a sodium storage anode material, the cycle performance of the CoS_2/C and CoS_2/C-600 anodes was measured at 100 mA g^{-1} (Fig. 7a). As a reference, pure CoS_2 without carbon matrix was obtained through first annealing of ZIF-67 in air and then sulfidation. Among the materials under investigation, the CoS_2/C polyhedrons exhibited the highest reversible capacities and most stable cycling performance. The reversible capacities always remained above 510 mA h g^{-1} during 100 cycles, corresponding to capacity retention of 90% calculated on the basis of the charge capacity of the 2nd cycle. Table S1† summarizes the electrochemical performance of some representative transition metal sulfide-based anodes in SIBs, demonstrating clear advantages of the CoS_2/C polyhedrons in this study.[12,48,49] On the contrary, the reversible capacities of the CoS_2/C-600 and pure CoS_2 both decreased sharply to go below 10 mA h g^{-1} in the first 60 cycles. In addition, rate capability is also a crucial feature to evaluate the electrochemical performance of an anode material. To highlight the role of sulfur heteroatom in improving the electrochemical performance, a CoS/C control sample was prepared using a sulfidation reaction of ZIF-67-derived CoO/C in a Na_2S solution (Fig. S8†).[26,50] In this process, the sulfidation reaction was operated at only 90 °C without a high-temperature heating, and thus the obtained carbon matrix was not doped with sulfur atom. The sample without S doping displayed relatively low reversible capacities and worse cycle stability compared with its counterpart with S doping, further proving the importance of sulphur heteroatom. From the rate capability tests shown in Fig. 7b, the average reversible capacities of the CoS_2/C polyhedrons were 455, 392, 356, 324, 307 and 288 mA h g^{-1} at the current densities of 200, 500, 800, 1000, 1500 and 2000 mA g^{-1}, respectively. Importantly, the specific capacities of more than 438 mA h g^{-1} still resumed when the current density was reduced back to 200 mA g^{-1}, suggesting the good structural robustness of the anode material. These electrochemical results clearly indicate that the optimal design of ultrafine nanoparticles with uniform dispersion and complete encapsulation in carbon matrix can greatly alleviate the mechanical stress to retain structural integrity and facilitate electron/ion transfer to enhance kinetic rate for Na-ions insertion/extraction, thus offering a stable cycling performance and good rate capability.

To better understand the different electrochemical behaviors between the CoS_2/C and CoS_2/C-600 electrodes, electrochemical impedance spectroscopy (EIS) measurements after a certain number of cycles in the fully charged state were carried out, and the results are shown as Nyquist plots in Fig. 8a and b. The Nyquist plots consisted of two partly compressed semicircles in medium-frequency region, followed by sloping lines in the low-frequency range. The plots were fitted by an equivalent electrical circuit presented in the inset of Fig. 8a and the best-fitted data were summarized in Table S2.† In the equivalent circuit, R_e denotes the ohm internal resistance, corresponding to the intercept on the real impedance axis at the high frequency end. The compressed semicircles were divided into two parts, R_f and R_{ct}, which represent the migration resistance of sodium ions passing the SEI film and the charge transfer resistance, respectively. Z_w refers to the Warburg impedance, associated with the Na-ions diffusion in the bulk electrode.[51,52] During cycling, the values of R_e for the two samples do not show any significant change, confirming the stability of internal resistance. It can be seen that both the R_f and R_{ct} values of the CoS_2/C and CoS_2/C-600 anodes markedly declined after first cycle and then increased in the subsequent cycles. The first decreased resistance can be

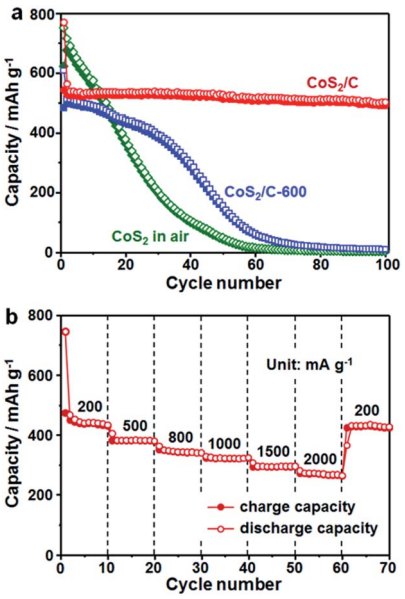

Fig. 7 (a) Comparison of cycle performance of the CoS_2/C, CoS_2/C-600 and CoS_2 obtained in air at a current density of 100 mA g^{-1}. (b) Rate capability tests of the CoS_2/C polyhedrons at various current densities.

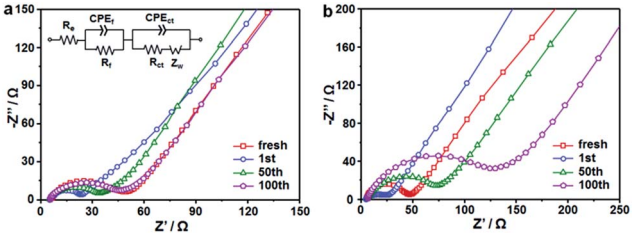

Fig. 8 Nyquist plots of (a) CoS_2/C polyhedrons and (b) CoS_2/C-600 electrodes after different cycles.

attributed to the transformation of CoS_2 particles into smaller nanocrystals and structural re-arrangement during first cycling.[26,53] This observation coincided well with the results of CVs and voltage profiles. Compared to the significant increase in CoS_2/C-600 electrode, the R_f and R_{ct} values of the CoS_2/C remained approximately unchanged for 100 cycles. Such behavior implies a stable electronic and ionic conductivity during long cycles, which is ascribed to the strain release from ultrafine nanoparticles and confinement effect of the carbon matrix, thereby further proving the structural robustness and interfacial stability of the CoS_2/C anode during repeated Na^+ insertion and extraction processes. The Z_w values in the CoS_2/C were also smaller than those in the CoS_2/C-600 during entire cycles, which confirms that reduced particle size can greatly enhance the diffusion kinetics of sodium ions in anode materials. Compared with the CoS_2/C, the EIS result of CoS/C control sample without S doping shows higher R_f and R_{ct} values, accounting for the enhanced interfacial stability and charge transfer ability of S heteroatom.

Furthermore, TEM technique was operated to directly observe the morphological changes of CoS_2/C anode after 100 full discharge/charge cycles (Fig. S9†). From the images, it can be seen that the original polyhedron shape with uniformly dispersed CoS_2 nanoparticles in carbon matrix was well maintained, again proving the good structural stability of the CoS_2/C polyhedrons during extended cycles for sodium ion storage. After cycling, there is a slight decrease in the amount of the doped heteroatoms due to the structured instability of active defects from these heteroatoms. However, the doped heteroatoms are still homogeneously distributed throughout the entire carbon matrix.

4. Conclusions

In summary, a type of dragon fruit-like nanostructure consisting of ultrafine CoS_2 nanoparticles uniformly encapsulated in N/S-doped carbon polyhedron has been successfully synthesized through the first decomposition of ZIF-67 precursor with optimizing pyrolysis temperature and subsequent sulfidation treatment. The pyrolysis temperature plays a key role in forming the uniformly dispersed, ultrafine CoS_2 nanoparticles. The co-doped heteroatoms come from the *in situ* carbonization of nitrogen-rich organic ligands in ZIF-67 and the following carbon–sulfur reaction during sulfidation treatment. It is proven that the integration of ultrafine and uniformly encapsulated active nanoparticles and N/S-doped carbon matrix can effectively guarantee enhanced reaction kinetics and a superior structural robustness against repeated sodium insertion/extraction. This designed material acting as an anode for SIBs exhibits a high reversible capacity (563 mA h g^{-1}), stable cycling performance (90% capacity retention after 100 cycles with a remained capacity of 510 mA h g^{-1}) and a good fast charge–discharge capability (307 and 288 mA h g^{-1} at large current densities of 1500 and 2000 mA g^{-1}, respectively). The current ZIF-derived strategy can be extended to the preparation of other dragon fruit-like metal compounds/carbon composites with high electrochemical performance for next-generation energy-storage devices, and materials for solar cells, catalysts and so on.

Acknowledgements

This study was supported by the Fundamental Research Funds for the Central Universities and the National Natural Science Foundation of China (No. 51502086).

Notes and references

1 N. Yabuuchi, K. Kubota, M. Dahbi and S. Komaba, *Chem. Rev.*, 2014, **114**, 11636–11682.
2 D. Kundu, E. Talaie, V. Duffort and L. F. Nazar, *Angew. Chem., Int. Ed.*, 2015, **54**, 3431–3448.
3 H. Kim, H. Kim, Z. Ding, M. H. Lee, K. Lim, G. Yoon and K. Kang, *Adv. Energy Mater.*, 2016, **6**, 1600943.
4 X. Li, G. Wu, X. Liu, W. Li and M. Li, *Nano Energy*, 2017, **31**, 1–8.
5 X. Li, Y. Feng, M. Li, W. Li, H. Wei and D. Song, *Adv. Funct. Mater.*, 2015, **25**, 6858–6866.
6 X. Li, W. Li, M. Li, P. Cui, D. Chen, T. Gengenbach, L. Chu, H. Liu and G. Song, *J. Mater. Chem. A*, 2015, **3**, 2762–2769.
7 W. Li, Y.-X. Yin, S. Xin, W.-G. Song and Y.-G. Guo, *Energy Environ. Sci.*, 2012, **5**, 8007–8013.
8 Z. Chen, Y. Yan, S. Xin, W. Li, J. Qu, Y.-G. Guo and W.-G. Song, *J. Mater. Chem. A*, 2013, **1**, 11404–11409.
9 H. Pan, Y.-S. Hu and L. Chen, *Energy Environ. Sci.*, 2013, **6**, 2338–2360.
10 W. Luo, F. Shen, C. Bommier, H. Zhu, X. Ji and L. Hu, *Acc. Chem. Res.*, 2016, **49**, 231–240.
11 Z. T. Shi, W. Kang, J. Xu, L. L. Sun, C. Wu, L. Wang, Y. Q. Yu, D. Y. W. Yu, W. Zhang and C. S. Lee, *Small*, 2015, **11**, 5667–5674.
12 F. Zhao, Q. Gong, B. Traynor, D. Zhang, J. Li, H. Ye, F. Chen, N. Han, Y. Wang, X. Sun and Y. Li, *Nano Res.*, 2016, **9**, 3162–3170.
13 X. Rui, H. Tan and Q. Yan, *Nanoscale*, 2014, **6**, 9889–9924.
14 X. Xu, W. Liu, Y. Kim and J. Cho, *Nano Today*, 2014, **9**, 604–630.
15 M. Mousa, Y. Oei and H. Richtering, *J. Phys., Colloq.*, 1980, **41**, 223–226.
16 X. Xie, T. Makaryan, M. Zhao, K. L. V. Aken, Y. Gogotsi and G. Wang, *Adv. Energy Mater.*, 2016, **6**, 1502161.
17 W. Luc and F. Jiao, *Acc. Chem. Res.*, 2016, **49**, 1351–1358.
18 M. Jin, S.-Y. Lu, L. Ma, M.-Y. Gan, Y. Lei, X.-L. Zhang, G. Fu, P.-S. Yang and M.-F. Yan, *J. Power Sources*, 2017, **341**, 294–301.
19 Z. Shadike, M. H. Cao, F. Ding, L. Sang and Z. W. Fu, *Chem. Commun.*, 2015, **51**, 10486–10489.
20 J. Zhou, N. Lin, W. Cai, C. Guo, K. Zhang, J. Zhou, Y. Zhu and Y. Qian, *Electrochim. Acta*, 2016, **218**, 243–251.
21 X. Liu, K. Zhang, K. Lei, F. Li, Z. Tao and J. Chen, *Nano Res.*, 2016, **9**, 198–206.
22 W.-H. Ryu, H. Wilson, S. Sohn, J. Li, X. Tong, E. Shaulsky, J. Schroers, M. Elimelech and A. D. Taylor, *ACS Nano*, 2016, **10**, 3257–3266.

23 P. Lou, Y. Tan, P. Lu, Z. Cui and X. Guo, *J. Mater. Chem. A*, 2016, **4**, 16849–16855.
24 Z. Zhang, Y. Gan, Y. Lai, X. Shi, W. Chen and J. Li, *RSC Adv.*, 2015, **5**, 103410–103413.
25 W. Shi, J. Zhu, X. Rui, X. Cao, C. Chen, H. Zhang, H. H. Hng and Q. Yan, *ACS Appl. Mater. Interfaces*, 2012, **4**, 2999–3006.
26 F. Han, C. Y. J. Tan and Z. Gao, *J. Power Sources*, 2017, **339**, 41–50.
27 X. Li, N. Fu, J. Zou, X. Zeng, Y. Chen, L. Zhou, W. Lu and H. Huang, *Electrochim. Acta*, 2017, **225**, 137–142.
28 J. Liu, C. Wu, D. Xiao, P. Kopold, L. Gu, P. A. Aken, J. Maier and Y. Yu, *Small*, 2016, **12**, 2354–2364.
29 N. L. Torad, M. Hu, S. Ishihara, H. Sukegawa, A. A. Belik, M. Imura, K. Ariga, Y. Sakka and Y. Yamauchi, *Small*, 2014, **10**, 2096–2107.
30 H. Hu, L. Han, M. Yu, Z. Wang and X. W. Lou, *Energy Environ. Sci.*, 2016, **9**, 107–111.
31 H. Li, Y. Sun, W. Sun and Y. Wang, *Adv. Funct. Mater.*, 2016, **26**, 8345–8353.
32 F. Han, C. Zhang, J. Yang, G. Ma, K. He and X. Li, *J. Mater. Chem. A*, 2016, **4**, 12781–12789.
33 L.-S. Zhang, W. Li, Z.-M. Cui and W.-G. Song, *J. Phys. Chem. C*, 2009, **113**, 20594–20598.
34 W. Li, L.-S. Zhang, Q. Wang, Y. Yu, Z. Chen, C.-Y. Cao and W.-G. Song, *J. Mater. Chem.*, 2012, **22**, 15342–15347.
35 L. Cao, D. Chen, W. Li and R. A. Caruso, *ACS Appl. Mater. Interfaces*, 2014, **6**, 13129–13137.
36 W. Li, D. Chen, F. Xia, J. Z. Y. Tan, P.-P. Huang, W.-G. Song, N. M. Nursam and R. A. Caruso, *Environ. Sci.: Nano*, 2016, **3**, 94–106.
37 S. Peng, X. Han, L. Li, Z. Zhu, F. Cheng, M. Srinivansan, S. Adams and S. Ramakrishna, *Small*, 2016, **12**, 1359–1368.
38 J. Jin, X. Zhang and T. He, *J. Phys. Chem. C*, 2014, **118**, 24877–24883.
39 Y. Du, X. Zhu, X. Zhou, L. Hu, Z. Dai and J. Bao, *J. Mater. Chem. A*, 2015, **3**, 6787–6791.
40 J. Xu, M. Wang, N. P. Wickramaratne, M. Jaroniec, S. Dou and L. Dai, *Adv. Mater.*, 2015, **27**, 2042–2048.
41 W. Li, M. Zhou, H. Li, K. Wang, S. Cheng and K. Jiang, *Energy Environ. Sci.*, 2015, **8**, 2916–2921.
42 Y. Liu, Y. Shen, L. Sun, J. Li, C. Liu, W. Ren, F. Li, L. Gao, J. Chen, F. Liu, Y. Sun, N. Tang, H. M. Cheng and Y. Du, *Nat. Commun.*, 2016, **7**, 10921.
43 C. Wu, J. Maier and Y. Yu, *Adv. Mater.*, 2016, **28**, 174–180.
44 X. Meng and D. Deng, *Chem. Mater.*, 2016, **28**, 3897–3904.
45 F. Zhao, Q. Gong, B. Traynor, D. Zhang, J. Li, H. Ye, F. Chen, N. Han, Y. Wang, X. Sun and Y. Li, *Nano Res.*, 2016, **9**, 3162–3170.
46 Y. Zhou, W. Sun, X. Rui, Y. Zhou, W. J. Ng, Q. Yan and E. Fong, *Nano Energy*, 2016, **21**, 71–79.
47 W. Li, C. Hu, M. Zhou, H. Tao, K. Wang, S. Cheng and K. Jiang, *J. Power Sources*, 2016, **307**, 173–180.
48 Y. N. Ko and Y. C. Kang, *Carbon*, 2015, **94**, 85–90.
49 Z. Che, Y. Li, K. Chen and M. Wei, *J. Power Sources*, 2016, **331**, 50–57.
50 F. Han, C. Zhang, B. Sun, W. Tang, J. Yang and X. Li, *Carbon*, 2017, **118**, 731–742.
51 A. A. AbdelHamid, X. Yang, J. Yang, X. Chen and J. Y. Ying, *Nano Energy*, 2016, **26**, 425–437.
52 L. Wu, H. Lu, L. Xiao, X. Ai, H. Yang and Y. Cao, *J. Power Sources*, 2015, **293**, 784–789.
53 J. S. Cho, S. Y. Lee and Y. C. Kang, *Sci. Rep.*, 2016, **6**, 23338.